Nanoscale

PAPER

View Article Online
View Journal | View Issue

Cite this: *Nanoscale*, 2024, **16**, 12957

g-C_3N_4 nanosheet supported $NiCo_2O_4$ nanoparticles for boosting degradation of tetracycline under visible light and ultrasonic irradiation†

Qingfeng Guo,‡[a,b] Changwang Yan,‡[a] Zhenqian Huang,[c] Yujie Liu,[c] Deshan Cheng,[a] Chaoyang Lu,[d] Jianhua Ran*[a,c] and Yingkui Yang *[a]

Received 12th April 2024,
Accepted 3rd June 2024

DOI: 10.1039/d4nr01611d

rsc.li/nanoscale

The doping of semiconductor materials through some facile and appropriate methods holds significant promise in enhancing the catalytic performance of catalysts. Herein, $NiCo_2O_4$/g-C_3N_4 composite catalysts were synthesized *via* a high-energy ball milling method. The microstructure and physicochemical characterization of the as-prepared composites confirmed the successful loading of $NiCo_2O_4$ nanoparticles onto the g-C_3N_4 nanosheets. The $NiCo_2O_4$/g-C_3N_4 composites showed excellent catalytic effect under visible light/ultrasonic irradiation, and the efficiency of tetracycline hydrochloride (TCH) degradation reached 90% within 15 min. The optical properties of g-C_3N_4 nanosheets were improved by doping, and the diffusion of active materials and carrier migration rate were improved by ultrasonic assistance. Possible catalytic mechanisms and potential pathways of the $NiCo_2O_4$/g-C_3N_4 composites for the degradation of TCH triggered by visible light/ultrasonic irradiation were proposed. This study provides a new strategy for energy-assisted photocatalytic degradation of organic pollutants.

1. Introduction

In recent years, a variety of antibiotics have been detected in surface water as emerging pollutants,[1–3] drawing increasing attention to the pollution of water by antibiotics. Tetracycline is one of the most commonly used antibiotics for treatment of diseases due to its broad-spectrum antimicrobial properties.[4,5] However, tetracycline cannot be fully absorbed, resulting in more than 70% being released into the environment. Tetracycline in water can also inhibit the normal growth of aquatic organisms and cause endocrine disorders in aquatic organisms.[6,7] In addition, the carcinogenic activity of tetracycline is very harmful to human health.[8] The existence of tetracycline in water damages water quality, posing a long-term potential threat to the ecosystem and human health. Therefore, how to remove tetracycline from water is an urgent problem to be solved.

Many efforts have been devoted to the degradation of tetracycline pollutants in water, such as adsorption,[9] advanced oxidation processes (AOPs),[10,11] and electrochemical[12] and catalytic degradation.[13–15] Among them, photocatalytic technology has attracted more attention owing to its effective utilization of sunlight. The band gap matching between a semiconductor material and solar energy is key to achieving efficient photocatalytic degradation. However, the lack of active sites and a high carrier recombination rate in semiconductor materials have greatly limited the development of photocatalytic technology. Ultrasonic technology is an emerging wastewater treatment solution with the advantages of high efficiency, fast speed and environmental protection.[16–18] The principle of ultrasonic catalysis technology is mainly based on the phenomenon of acoustic cavitation. Cavitation bubbles are first formed on the catalyst surface through ultrasonic waves, and then the local high temperature and high pressure caused by the rupture of cavitation bubbles will promote the formation of strongly oxidizing monomers such as hydroxyl free radicals.[19,20] The combination of ultrasonic waves and photocatalysis has enhanced the degradation of organic pollutants, overcoming the limitations of any single degradation method. The use of ultrasonic wave vibration results in more strongly

[a]*State Key Laboratory of New Textile Materials and Advanced Processing Technologies, Wuhan Textile University, Wuhan 430200, China. E-mail: ykyang@wtu.edu.cn*
[b]*Engineering Research Center for Clean Production of Textile Dyeing and Printing, Ministry of Education, Wuhan Textile University, Wuhan 430200, China*
[c]*Hubei Key Laboratory of Biomass Fiber and Ecological Dyeing and Finishing, Wuhan Textile University, Wuhan 430020, China. E-mail: jhran@wtu.edu.cn*
[d]*Qianshui (Hubei) Environmental Technology Co., Ltd, Tianmen 431700, China*
†Electronic supplementary information (ESI) available. See DOI: https://doi.org/10.1039/d4nr01611d
‡These authors equally contributed to this work.

oxidizing monomers, with an enhanced diffusion rate and a mass transfer effect in the liquid phase. As a result, the contact frequency and reaction rate of the photocatalyst and organic pollutant will be improved, so will the catalytic degradation effect.

As a typical polymer photocatalyst with non-toxicity, low cost, easy availability and high conductivity, graphitized carbon nitride (g-C_3N_4) is widely applied in photocatalytic degradation.[21–24] Moreover, g-C_3N_4 with a two-dimensional layered structure has a high piezoelectric coefficient.[25,26] However, its still face limitations such as low potential energy and easy recombination of electron-hole pairs.[27,28] Thus, metals and non-metals have been doped in g-C_3N_4 to improve its photocatalytic performance. Different techniques have been adopted for g-C_3N_4 doping, such as thermal polycondensation synthesis,[29] solid phase synthesis,[30] a solvothermal method,[31] and ball milling.[32,33] Among them, the ball milling technique is the most suitable method for scaled production because it is simple, efficient and does not require organic solvents. More importantly, the ball milling method can significantly enhance the active sites and stability of nanocatalysts, ideal for the preparation of highly efficient nanocatalysts.

In this study, the $NiCo_2O_4$/g-C_3N_4 composite catalysts were synthesized *via* a high-energy ball milling method. $NiCo_2O_4$ nanoparticle doping improved the band-gap structure of g-C_3N_4 and enhanced the absorption of visible light, providing a way for electron transfer and enhancing the separation efficiency of photogenerated carriers. The microstructure and physicochemical properties of $NiCo_2O_4$/g-C_3N_4 composites were studied, and the catalytic activity and the mechanism of the composite catalysts under different catalytic conditions were investigated. The as-prepared $NiCo_2O_4$/g-C_3N_4 composite catalysts showed excellent catalytic activity under the synergistic effect of visible light/ultrasonic irradiation, suggesting that ball milling is a simple and reliable method for large-scale synthesis of nanocatalysts. This work has great practical application value for highly efficient degradation of organic pollutants in wastewater.

2. Experimental

2.1. Materials

Urea, cobalt(II) nitrate hexahydrate, nickel(II) nitrate hexahydrate, sodium hydroxide and tetracycline hydrochloride (TCH) were supplied by Sinopharm Chemical Reagent Co., Ltd (Shanghai, China).

2.2. Preparation of g-C_3N_4

10 g of urea and 30 mL of deionized water were mixed followed by drying. After drying, the mixture was transferred to a 100 mL muffle furnace for calcination at 550 °C for 3 h with a heating rate of 5 °C min^{-1}.

2.3. Preparation of $NiCo_2O_4$

The co-precipitation method was used to synthesize $NiCo_2O_4$ nanoparticles. 0.87 g of Ni $(NO_3)_2{\cdot}6H_2O$ and 3.49 g of Co $(NO_3)_2{\cdot}6H_2O$ were dissolved in 50 mL of deionized water with a molar ratio of 1 : 4. After stirring for 1 h, 25 mL of 2 M NaOH was added to the mixture solution, and a large amount of Ni–Co hydroxide coprecipitate was rapidly formed. The coprecipitate was filtered and washed with water and then dried overnight at 60 °C. Finally, the powder was calcined at 300 °C for 3h in air with a heating rate of 6 °C min^{-1}.

2.4. Preparation of $NiCo_2O_4$/g-C_3N_4

The $NiCo_2O_4$/g-C_3N_4 composite catalysts were prepared *via* a high-energy ball milling method, as shown schematically in Fig. 1. In a typical synthesis process, different mass ratios of $NiCo_2O_4$ and g-C_3N_4 were placed in a planetary ball milling machine in 250 mL zirconia jars, and 200 g of different sized zirconia balls were added to each jar. After that, the high energy ball milling machine was run at a rotational speed of 500 rpm for 6 h. The obtained powder was finally dried overnight at 60 °C.

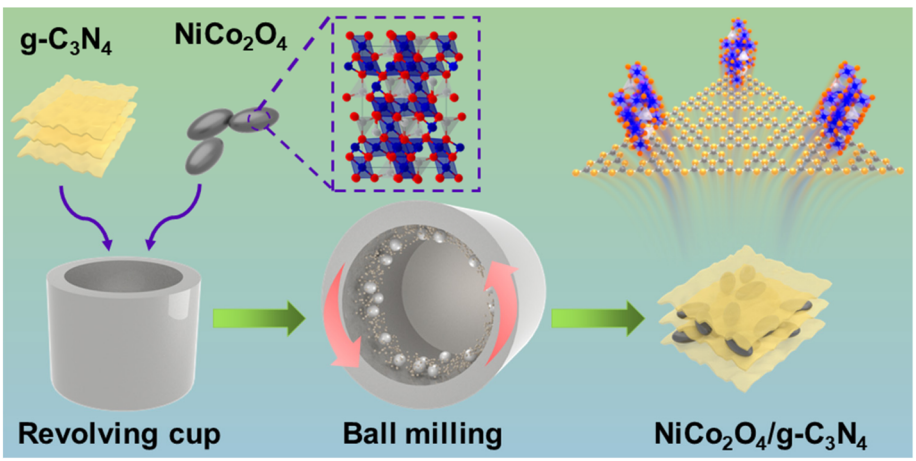

Fig. 1 Schematic illustration of the preparation of $NiCo_2O_4$/g-C_3N_4 composites.

2.5. Characterization

The surface morphology and elemental composition of the g-C_3N_4 samples were analyzed by transmission electron microscopy (TEM, Tecnai G220S-TWIN, FEI Co., Ltd, USA) with energy-dispersive X-ray spectroscopy (EDX, Oxford, UK). The chemical structure of samples was analyzed by Fourier transform infrared spectroscopy (FTIR, TENSOR 27, Bruker, USA) in the frequency range of 500–4000 cm^{-1}. The crystal structure of the samples was analyzed using an X-ray diffractometer (XRD, D/max 2500, Rigaku, Japan) within the 2θ range from 10° to 70°. The specific surface area of g-C_3N_4 and $NiCo_2O_4$/g-C_3N_4 composites was obtained from a Micromeritics TriStar II 3020 sorption analyzer (Micromeritics Instrument Co., USA). The chemical composition of $NiCo_2O_4$/g-C_3N_4 composites was recorded by X-ray photoelectron spectroscopy (XPS, PHI-5000C ESCA, PerkinElmer, USA).

2.6. Catalytic activity measurements

Tetracycline solution was employed to evaluate the catalytic activity of the $NiCo_2O_4$/g-C_3N_4 composite catalysts. 50 mg of catalyst were added to the tetracycline solution (50 mL, 5 mg L^{-1}) under simultaneous xenon lamp (λ >420 nm) irradiation and ultrasound actuation. The degradation degree of the tetracycline solution at different time intervals was measured by UV-vis spectroscopy (Analytik, Jena, Spe cord 210 plus). The test was adjusted accordingly to examine the effect of the amount of $NiCo_2O_4$ and catalytic conditions.

2.7. Electrochemical test

The electrochemical performance of the $NiCo_2O_4$/g-C_3N_4 composites was analyzed on an electrochemical workstation (CorrTest CS 310, Wuhan, China) through a standard three-electrode system. The working electrode was prepared as follows: 10 mg of catalyst was mixed with 1 mL of 5 wt% Nafion solution followed by deposition on a fluorine-doped tin oxide (FTO) glass and drying in air. 0.1 M Na_2SO_4 solution was used as the electrolyte, while Ag/AgCl and a Pt slice were used as the reference electrode and counter electrode, respectively. EIS measurements were performed using the same system over a frequency range of 10^5–10^{-2} Hz with an AC amplitude of 0.27 V at the open circuit potential.

3. Results and discussion

3.1. Characterization

The color of the g-C_3N_4 powder changed from yellow to gray after the introduction of $NiCo_2O_4$ nanoparticles, as shown in Fig. 2a. The TEM images of g-C_3N_4 nanosheets showed a 2D thin nanosheet with a wrinkle-like structure (Fig. 2b). The TEM image (Fig. 2c) demonstrates that $NiCo_2O_4$ nanoparticles are well embedded on the surface of g-C_3N_4 nanosheets after doping with nanoparticles. At a higher magnification, the surface shows many elliptical $NiCo_2O_4$ nanoparticles, as shown by the red circles in Fig. 2d. Besides, the HRTEM image of the lattice fringe shows a separation of 0.25 nm (Fig. 2e), corresponding to the (311) plane of the $NiCo_2O_4$ phase.[34,35] The EDS elemental mapping in Fig. 2f displays that $NiCo_2O_4$/g-C_3N_4 composites are composed of C, O, N, Ni and Co elements. The distribution of Ni and Co elements is clearly visible with an elliptical shape, indicating that $NiCo_2O_4$ nanoparticles have been successfully loaded onto g-C_3N_4 nanosheets.

The FT-IR spectra of g-C_3N_4 samples are shown in Fig. 3a. For original g-C_3N_4 and $NiCo_2O_4$/g-C_3N_4 composites, the vibration peak at 807 cm^{-1} was assigned to the tri-s-triazine unit structure of g-C_3N_4. The wide absorption peaks in the range of 1200–1800 cm^{-1} were ascribed to CN heterocycle skeletal vibration. The broad absorption peaks at 2900–3300 cm^{-1}

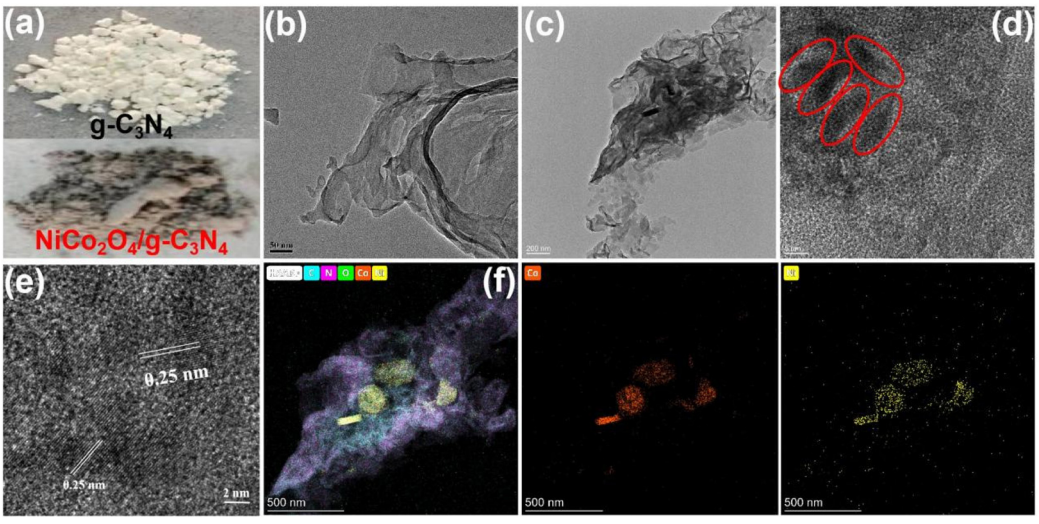

Fig. 2 Optical photos (a) and TEM images of g-C_3N_4 nanosheets and $NiCo_2O_4$/g-C_3N_4 composites at different magnifications (b–d), HRTEM image (e) of $NiCo_2O_4$/g-C_3N_4 composites and the corresponding elemental mapping (f).

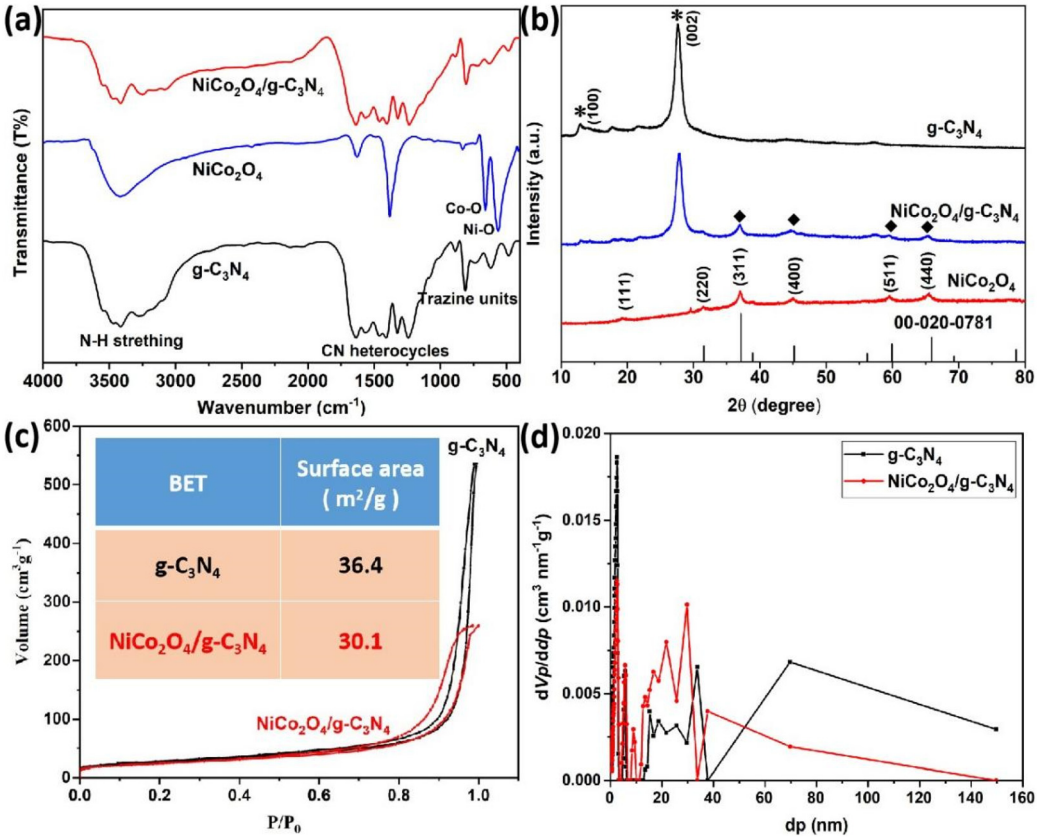

Fig. 3 FT-IR spectra (a) and XRD pattern (b) of g-C_3N_4, $NiCo_2O_4$ and $NiCo_2O_4$/g-C_3N_4. The adsorption–desorption isotherm curves (c) and porosity scale distribution (d) of g-C_3N_4 and $NiCo_2O_4$/g-C_3N_4.

were due to N–H stretching.[36] In the FT-IR spectra of $NiCo_2O_4$ nanoparticles, there are two strong metal–oxygen peaks at 659.6 and 563.2 cm^{-1} corresponding to Co–O and Ni–O, respectively.[37] However, the metal–oxygen peaks were not detected in $NiCo_2O_4$/g-C_3N_4 composites, which may be due to the small amount of $NiCo_2O_4$ nanoparticles and their heterogeneous dispersion on the g-C_3N_4 surface.

The crystal structure of g-C_3N_4, $NiCo_2O_4$ and $NiCo_2O_4$/g-C_3N_4 composites was studied by XRD (Fig. 3b). The XRD pattern of $NiCo_2O_4$ nanoparticles displays six characteristic peaks at 2θ = 19.8°, 31.1°, 36.6°, 44.6°, 59.1° and 64.9° corresponding to the (111), (220), (311), (400), (511) and (440) planes, respectively. These peaks match the standard JCPDS of $NiCo_2O_4$ (No. 20-0781).[38] The XRD patterns of g-C_3N_4 and $NiCo_2O_4$/g-C_3N_4 composites show two peaks at 13.0° and 27.5° corresponding to the (100) and (002) planes of g-C_3N_4 (marked with *). In addition, $NiCo_2O_4$/g-C_3N_4 composites exhibit $NiCo_2O_4$ characteristic peaks (marked with ◆), indicating that $NiCo_2O_4$ has been successfully loaded onto g-C_3N_4 nanosheets.

The pore size distribution of the original g-C_3N_4 and $NiCo_2O_4$/g-C_3N_4 composites was further analyzed using the N_2 adsorption/desorption isotherm (Fig. 3c). Both samples display a type IV isotherm with a H3 hysteresis loop. The surface area of the $NiCo_2O_4$/g-C_3N_4 composites was calculated to be 30.1 $m^2\ g^{-1}$ (Fig. 3c inset), which is a little less than that of g-C_3N_4 (36.4 $m^2\ g^{-1}$). This may be due to the introduction of $NiCo_2O_4$ nanoparticles which have filled the pores of g-C_3N_4 nanosheets. In addition, the pore size distribution of $NiCo_2O_4$/g-C_3N_4 composites as shown in Fig. 3d further suggests a mesoporous structure of the composites.

The chemical composition of the $NiCo_2O_4$/g-C_3N_4 composites was analyzed by XPS. The XPS wide scan spectrum of the composites (Fig. 4a) is composed of five elements (Ni, Co, O, C and N), where Ni and Co elements are derived from metal oxides and the N element from g-C_3N_4 nanosheets. In the Co 2p spectra, two kinds of Co species and two shakeup satellites were detected as shown in Fig. 4b. The peaks at 782.6 and 797.4 eV are assigned to Co^{2+}, and the peaks at 780.3 and 795.4 eV to Co^{3+}. In the Ni 2p spectra (Fig. 4c), the high-resolution spectrum of Ni 2p can be fit to two spin–orbit doublets characteristic of Ni^{2+} (857.7 and 875.7 eV) and Ni^{3+} (855.7and 873.3 eV). The peaks located at around 862.1 and 880.4 eV are indexed to the two shake-up satellites of nickel.[39] The O 1s high-resolution spectra (Fig. 4d) are separated into three peaks at 529.4, 530.8 and 532.6 eV, attributed to metal oxygen bonds, adsorbed water on the surface and the hydroxyl group, respectively. The C 1s XPS peaks at 285.3, 286.8 and 288.8 eV are attributed to graphitic carbon (C–C), C–N bonds and the sp^2-hybridized carbon bond, respectively (Fig. 4e).[40] In Fig. 4f, for N 1s, the three peaks located at 398.6, 399.8 and 401.2 eV are

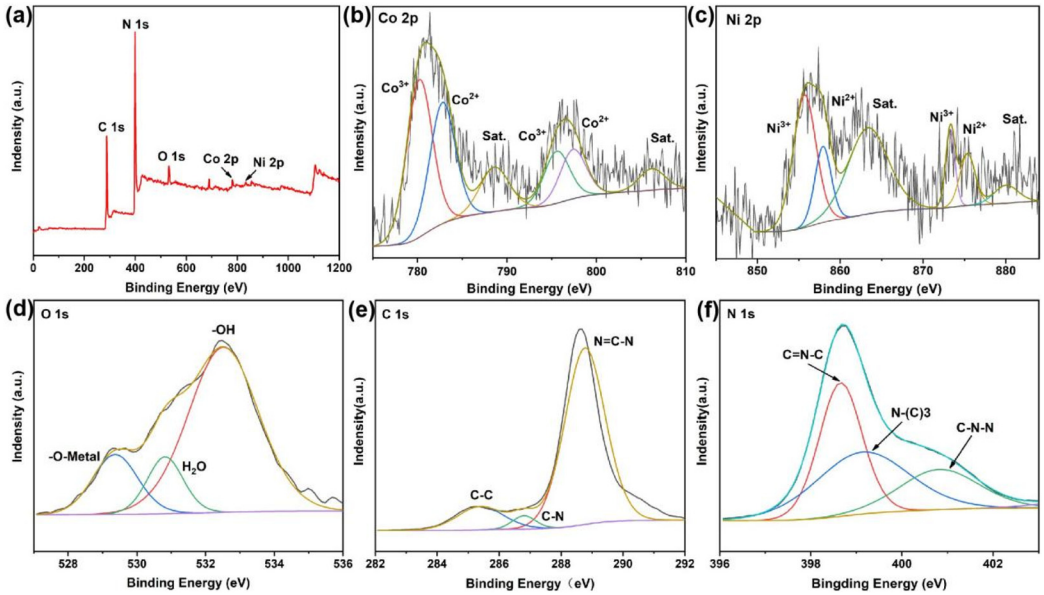

Fig. 4 Wide-scan XPS spectra of $NiCo_2O_4$/g-C_3N_4 composites (a) and detailed resolution of Co 2p, Ni 2p, O 1s, C 1s, and N 1s peaks (c–f).

ascribed to sp2-hybridized nitrogen (C═N–C), sp^3-hybridized nitrogen (N–$(C)_3$) and amino functional group coupled carbon (C–N–H), respectively.[41] The XPS spectra further demonstrated that the $NiCo_2O_4$ nanoparticles were successfully anchored onto the g-C_3N_4 nanosheets.

3.2. Optical properties

The optical properties of the g-C_3N_4, $NiCo_2O_4$ and $NiCo_2O_4$/g-C_3N_4 samples were analyzed using UV–vis spectra. Fig. 5a shows that the absorption peak of pure g-C_3N_4 decreases rapidly after 400 nm, indicating a narrow visible-light response range. In sharp contrast, $NiCo_2O_4$ nanoparticles present a wide absorption spectrum in the visible-light region. As a result, the $NiCo_2O_4$/g-C_3N_4 composites also exhibit a wide absorption spectrum from the UV to visible-light region.

The optical band gap of the samples can be estimated from Tauc plots following the equation:[42]

$$(ah\nu) = A(h\nu - E_g)^{1/2} \quad (1)$$

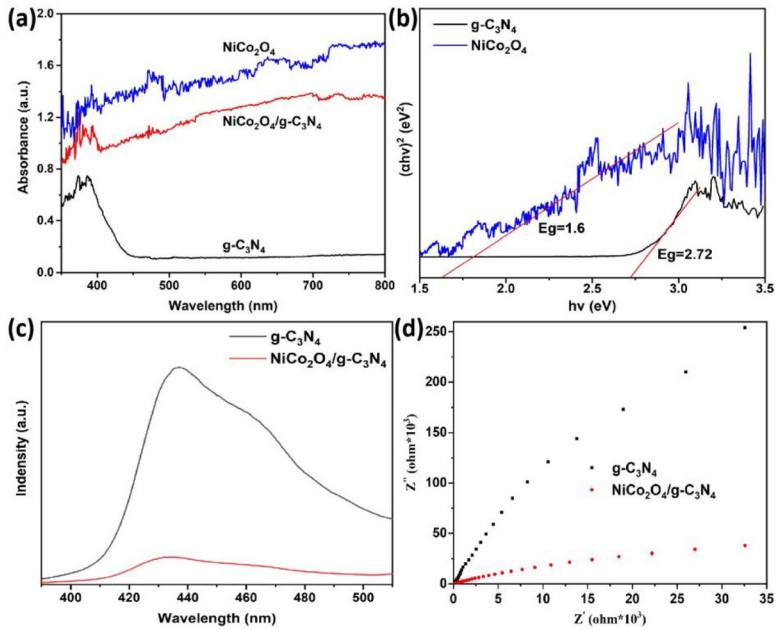

Fig. 5 UV–vis spectra (a) and the corresponding Tauc plots (b) of g-C_3N_4, $NiCo_2O_4$ and $NiCo_2O_4$/g-C_3N_4 composites. PL spectra (c) and EIS Nyquist plots (d) of g-C_3N_4 and $NiCo_2O_4$/g-C_3N_4 composites.

where a, ν, E_g and A represent the absorption coefficient, light frequency, band gap energy and proportionality constant, respectively.

From the estimated results in Fig. 5b, the band gaps of g-C_3N_4 and $NiCo_2O_4$ were determined to be 2.72 and 1.60 eV, respectively. The small energy gap will facilitate the absorption of visible light, resulting in excellent photocatalytic properties of $NiCo_2O_4$/g-C_3N_4 composites.

The high photogenerated electron–hole pair recombination rate is one of the main factors hindering the development of photocatalysis technology. Photoluminescence (PL) properties of g-C_3N_4 and $NiCo_2O_4$/g-C_3N_4 composites were analyzed by spectral resolution spectroscopy. Fig. 5c shows that the photoluminescence intensity of $NiCo_2O_4$/g-C_3N_4 is lower than that of g-C_3N_4. The decrease of PL intensity indicates that the doping with nanoparticles promotes efficient electron–hole separation and inhibits the carrier recombination process, resulting in an enhanced photocatalytic efficiency of the $NiCo_2O_4$/g-C_3N_4 composites.

The electrochemical performance of the samples was measured by electrochemical impedance spectroscopy (EIS) in a 0.1 M Na_2SO_4 solution. The semicircle radius of $NiCo_2O_4$/g-C_3N_4 composites was significantly smaller than that of pure g-C_3N_4 (Fig. 5d). It is well known that the smaller the semicircle in the EIS Nyquist plot, the faster the charge transfer rate and the lower the electron–hole recombination rate. This is mainly due to the excellent conductivity of $NiCo_2O_4$ nanoparticles, which act as a bridge for electron transfer and promote the migration of charge carriers.

3.3. Photocatalytic activity

A tetracycline aqueous solution (5 mg L^{-1}) was employed to evaluate the catalytic activity of the $NiCo_2O_4$/g-C_3N_4 composites. The effects of ultrasonic power, content of $NiCo_2O_4$ and illumination on the catalytic performance of the composites were investigated. It can be seen from the experimental results that the degradation rate decreases slightly without light irradiation (Fig. S1†). This is because the catalyst sample was placed in the solution at this stage, and the dye molecules were adsorbed onto the surface to reach an adsorption equilibrium. As shown in Fig. 6a, when the ultrasonic power was 150 W, the ultrasonic degradation efficiency of the $NiCo_2O_4$/g-C_3N_4 composites was 70%. The degradation efficiency slightly increased when the power was 250 W. With a further increase of ultrasonic power to 400 W, the ultrasonic degradation rate significantly increased with the degradation efficiency reaching 80% within 15 min. These findings suggest that the ultrasonic power has a direct impact on the degradation efficiency. The increase in ultrasonic power will increase the energy of cavitation, leading to more cavitation bubbles and active free radicals. At the same time, ultrasonic

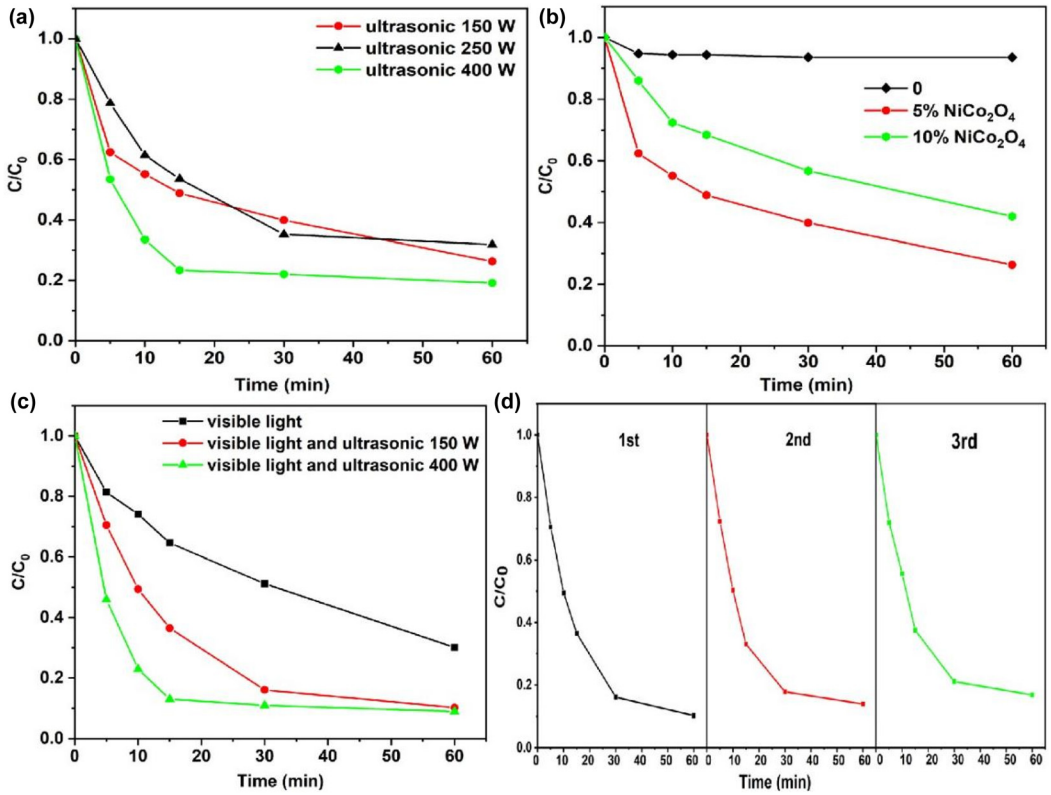

Fig. 6 Decomposition of residuary TCH solution by $NiCo_2O_4$/g-C_3N_4 composites under different ultrasonic powers (a), different contents of $NiCo_2O_4$ (b) and different illumination conditions (c); stability of the $NiCo_2O_4$/g-C_3N_4 composite catalyst (d).

waves accelerate the carrier migration rate and reduce the electron–hole recombination.

The stability of photocatalysts has been considered as an essential aspect for their practical applications. The photocatalytic cyclability of the $NiCo_2O_4$/g-C_3N_4 composites was studied by a cycling test. As shown in Fig. 6d, the photocatalytic activity rate exhibits good stability after three cycles, which has proved the good stability of the $NiCo_2O_4$/g-C_3N_4 composite catalyst. Moreover, the XRD pattern of the $NiCo_2O_4$/g-C_3N_4 composite catalyst remains basically unchanged after the reaction (Fig. S2†), indicating the good stability of the catalyst.

Here, the efficiency comparison of the g-C_3N_4 composite catalyst for degradation of TCH is listed in Table S1.† As can be seen from Table S1,† the catalytic efficiency could be significantly increased through the synergistic effect of ultrasound and illumination.

3.4. Catalytic mechanism

The generated main active species during the catalytic process were investigated by electron paramagnetic resonance spectroscopy. 5,5-Dimethy-1-pyrroline-*N*-oxide (DMPO) as the most frequently used spin trapping agent was employed for the detection of reactive oxygen radicals.[43] As shown in Fig. S3,† when the $NiCo_2O_4$/g-C_3N_4 composite was exposed to visible light, typical patterns of both DMPO-$^{\bullet}O_2^-$ (Fig. S3a†) and DMPO-$^{\bullet}$OH (Fig. S3b†) were observed in the EPR spectrum, indicating the generation of reactive oxygen species (ROS) during the photosensitizing process of the $NiCo_2O_4$/g-C_3N_4 composite under visible light irradiation.

The possible catalytic mechanism of $NiCo_2O_4$/g-C_3N_4 composites under the combination of visible light and ultrasonic irradiation is shown in Fig. 7. $NiCo_2O_4$ doping improves the optical properties of g-C_3N_4 nanosheets, resulting in a smaller band gap of $NiCo_2O_4$/g-C_3N_4 composites with increased utilization of light energy. Besides, the metal compounds have good electrical conductivity to promote the efficient separation of electron–hole pairs. Meanwhile, ultrasonic waves accelerate the carrier migration rate and promote the diffusion of oxygen to the surface of the catalyst, resulting in more active free radicals due to electrons combining with oxygen molecules. When the two semiconductors with different Fermi levels come into contact with each other, e^- will flow from g-C_3N_4 with a higher Fermi level to $NiCo_2O_4$, and h^+ will flow from $NiCo_2O_4$ with a lower Fermi level to g-C_3N_4, resulting in a built-in electric field (as shown in Fig. 7). However, the CB base of g-C_3N_4 forms upward "spikes" at the interface and barrier region, which will hinder the migration of electrons (e^-) from the CB of $NiCo_2O_4$ to the CB of g-C_3N_4. In addition, the Coulomb repulsion at the interface can also hinder the migration of photogenerated carriers.[44,45] Based on the above discussion, both g-C_3N_4 and $NiCo_2O_4$ can be excited to produce photogenic e^- and holes (h^+) under light irradiation. Some e^- in the CB of g-C_3N_4 and h^+ in the VB of $NiCo_2O_4$ recombine in the space charge region as a result of the interaction between the built-in electric field, band bending and

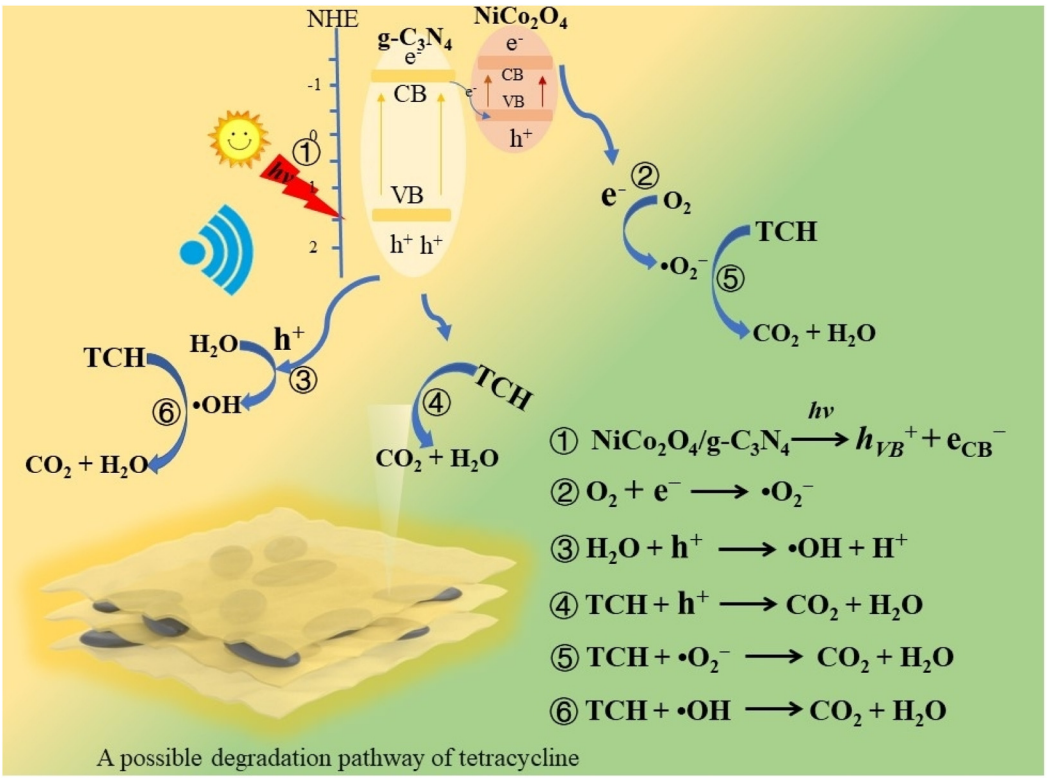

Fig. 7 Possible catalytic mechanism of $NiCo_2O_4$/g-C_3N_4 composites under the synergistic effect of visible light and ultrasonic irradiation.

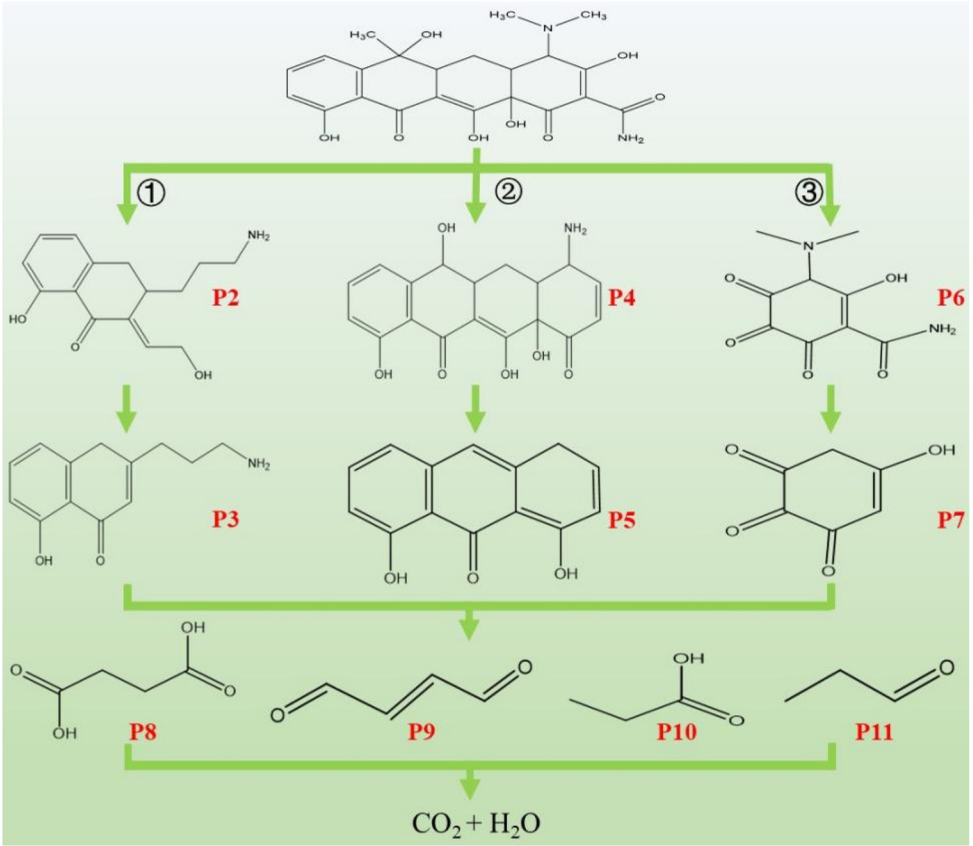

Fig. 8 Possible degradation pathways of tetracycline hydrochloride through the $NiCo_2O_4$/g-C_3N_4 composite system.

Coulomb repulsion. At the same time, e^- in the CB of $NiCo_2O_4$ and h^+ in the VB of g-C_3N_4 will be retained and react with O_2 and H_2O, respectively, to form superoxide radicals ($^{\bullet}O_2^-$) and hydroxyl radicals ($^{\bullet}OH$). Due to the combined involvement of active free radicals such as h^+, $^{\bullet}O_2^-$ and $^{\bullet}OH$, TCH is eventually degraded into CO_2 and H_2O (as shown in eqn ①–⑥). In summary, $NiCo_2O_4$/g-C_3N_4 composites have excellent catalytic performance under the synergistic effect of visible light and ultrasonic irradiation.

3.5. Potential TCH degradation pathways

The most common degradation pathways of tetracycline hydrochloride include demethylation, dehydroxylation, deamination and ring-opening.[46,47] Three possible degradation pathways are shown in Fig. 8. In pathway ①, the tetracycline molecule loses the hydroxyl and methyl groups, thus opening the ring to form P2. The branched double bond of P2 is subsequently broken by oxidation to obtain P3. In pathway ②, the tetracycline molecule loses $-CONH_2$ and $-CH_3$ to obtain P4, which is then converted to P5 by a ring-opening reaction. In pathway ③, the third six-membered ring of tetracycline is oxidized to form P6, which is then transformed to P7 by the removal of $-N(CH_3)_2$ and $-CONH_2$. Furthermore, small molecule intermediates (P8, P9, P10 and P11) can be further oxidized by the above three pathways. Finally, all the intermediates are eventually oxidized to CO_2 and H_2O under the action of reactive oxygen species. In summary, the $NiCo_2O_4$/g-C_3N_4 composite system does not produce any dangerous compounds during the TCH degradation process.

4. Conclusions

$NiCo_2O_4$ nanoparticles were successfully loaded onto the g-C_3N_4 nanosheet surface by a facile ball milling process. The doping with $NiCo_2O_4$ improved the optical properties of g-C_3N_4 with a narrower band gap, resulting in an enhanced efficiency in utilization of visible light. The metal compounds introduced new pathways for electron transfer and hence improved the efficiency of photogenerated carrier separation. The results demonstrated that the catalytic efficiency of $NiCo_2O_4$/g-C_3N_4 composite catalysts under the synergistic effect of visible light and ultrasonic irradiation was much higher than that of a single effect. Ultrasonic waves accelerated the carrier migration rate with enhanced diffusion of oxygen to the catalyst surface, resulting in more active free radicals. Possible catalytic mechanisms and potential pathways for the degradation of tetracycline hydrochloride have been proposed. The ultrasonic assisted photocatalysis demonstrated to be an environmentally friendly catalytic technology with a wide application prospect in the field of pollution control.

Conflicts of interest

The authors declare that the publication of this paper has no conflicts of interest.

Acknowledgements

This research was supported by the financial support of National Science Foundation (No. 62101391), Unveiled Projects of Department of Science and Technology of Hubei Province (2023BEB041), Open Subject of Engineering Research Center for Clean Production of Textile Printing and Dyeing, and Open Subject of Hubei Provincial Engineering Center of Industrial Fiber Preparation and Application (FZXCL202307, FZXCL202318).

References

1 C. Yang, G. Song and W. Lim, A review of the toxicity in fish exposed to antibiotics, *Comp. Biochem. Physiol., Part C: Toxicol. Pharmacol.*, 2020, **237**, 108840.
2 M. D. Barton, Antibiotic use in animal feed and its impact on human health, *Nutr. Res. Rev.*, 2000, **13**(2), 279–299.
3 F. R. Ungemach, D. Müller-Bahrdt and G. Abraham, Guidelines for prudent use of antimicrobials and their implications on antibiotic usage in veterinary medicine, *Int. J. Med. Microbiol.*, 2006, **296**, 33–38.
4 Y. Zhou, Y. Gao and J. Jiang, Transformation of tetracycline antibiotics during water treatment with unactivated peroxymonosulfate, *Chem. Eng. J.*, 2020, **379**, 122378.
5 Y. Kuang, H. Jia and K. Miyanaga, Effect of milk on antibacterial activity of tetracycline against Escherichia coli and Staphylococcus aureus isolated from bovine mastitis, *Appl. Microbiol. Biotechnol.*, 2009, **84**, 135–142.
6 L. Xu, H. Zhang and P. Xiong, Occurrence, fate, and risk assessment of typical tetracycline antibiotics in the aquatic environment: A review, *Sci. Total Environ.*, 2021, **753**, 141975.
7 D. Cheng, H. H. Ngo and W. Guo, A critical review on antibiotics and hormones in swine wastewater: Water pollution problems and control approaches, *J. Hazard. Mater.*, 2020, **387**, 121682.
8 N. Al-Waili, K. Salom and A. Al-Ghamdi, Antibiotic, pesticide, and microbial contaminants of honey: human health hazards, *Sci. World J.*, 2012, **2012**, 1–9.
9 D. Qiao, Z. Li and J. Duan, Adsorption and photocatalytic degradation mechanism of magnetic graphene oxide/ZnO nanocomposites for tetracycline contaminants, *Chem. Eng. J.*, 2020, **400**, 125952.
10 J. Fan, J. Liu and Y. Cai, Efficient degradation of tetracycline in FeS-based SR-AOPs process at basic pHs: The overlooked role of metal complexation and redox reaction in persulfate activation, *Chem. Eng. J.*, 2023, **466**, 143168.
11 R. Duan, S. Ma and S. Xu, Soybean straw biochar activating peroxydisulfate to simultaneously eliminate tetracycline and tetracycline resistance bacteria: Insights on the mechanism, *Water Res.*, 2022, **218**, 118489.
12 M. Ebratkhahan, M. Zarei and N. Arsalani, Facile synthesis and preparation of graphite/chitosan/graphene quantum dots nanocomposite cathode for electrochemical removal of tetracycline from aqueous solution, *Sep. Purif. Technol.*, 2022, **299**, 121663.
13 X. Wang, J. Li, K. Chen, J. Li, Y. Jia, Q. Mei and Q. Wang, Facile synthesis of oxygen vacancies enriched ZnFe2O4 for effective photocatalytic peroxodisulfate activation, *Sep. Purif. Technol.*, 2022, **303**, 122205.
14 Z. Cao, Y. Jia, Q. Wang and H. Cheng, High-efficiency photo-Fenton Fe/g-C_3N_4/kaolinite catalyst for tetracycline hydrochloride degradation, *Appl. Clay Sci.*, 2021, **212**, 106213.
15 L. Wang, X. Ma, G. Huang, R. Lian, J. Huang, H. She and Q. Wang, Construction of ternary CuO/$CuFe_2O_4$/g-C_3N_4 composite and its enhanced photocatalytic degradation of tetracycline hydrochloride with persulfate under simulated sunlight, *J. Environ. Sci.*, 2022, **112**, 59–70.
16 J. Jiang, S. Liu, D. Shi, T. Sun, Y. Wang, S. Fu, Y. Liu, M. Li, D. Zhou and S. Dong, Spin state-dependent in situ photo-Fenton-like transformation from oxygen molecule towards singlet oxygen for selective water decontamination, *Water Res.*, 2023, **244**, 120502.
17 J. Jiang, Z. Zhao, J. Gao, T. Li, M. Li, D. Zhou and S. Dong, Nitrogen vacancy-modulated peroxymonosulfate nonradical activation for organic contaminant removal via high-valent cobalt-oxo species, *Environ. Sci. Technol.*, 2022, **56**, 5611–5619.
18 B. Janani, A. Syed, H.A. Al-Shwaiman, M.M. Alkhulaifi, A. M. Elgorban and S.S. Khan, Performance analysis of novel $Bi_6Cr_2O_{15}$ coupled Co_3O_4 nano-heterostructure constructed by ultrasonic assisted method: Visible-light driven photocatalyst and antibacterial agent, *Colloids Surf., A*, 2021, **622**, 126671.
19 Y. Mao, B. Qiu, P. Li, X. Liu and S.M. Chen, Ultrasonic-assisted synthesis $Zn_{0.78}Cd_{0.22}S/Bi_2MoO_6$ heterojunction to improve photocatalytic performance for hexavalent chromium removal and hydrogen peroxide production, *Colloids Surf., A*, 2022, **648**, 129363.
20 F. Niu, Y. Li, C. Song, X. Yan and Z. Zhang, Microstructure and Wear Resistance of TiCp/Ti6Al4V Composite Coatings by Follow-Up Ultrasonic-Assisted Laser Additive Manufacturing, *Coatings*, 2022, **12**(7), 986.
21 H. Liu, J. Liang, S. Fu, L. Li, J. Cui, P. Gao and J. Zhou, N doped carbon quantum dots modified defect-rich g-C_3N_4 for enhanced photocatalytic combined pollutions degradation and hydrogen evolution, *Colloids Surf., A*, 2020, **591**, 124552.
22 S. Chinnapaiyan, T.W. Chen, S.M. Chen, Z.A. Alothman, M. A. Ali, S.M. Wabaidur and W.H. Chang, Ultrasonic-assisted preparation and characterization of magnetic $ZnFe_2O_4$/g-C_3N_4 nanomaterial and their applications towards

electrocatalytic reduction of 4-nitrophenol, *Ultrason. Sonochem.*, 2020, **68**, 105071.

23 Y. Shi, L. Li and H. Sun, Engineering ultrathin oxygen-doped g-C_3N_4 nanosheet for boosted photoredox catalytic activity based on a facile thermal gas-shocking exfoliation effect, *Sep. Purif. Technol.*, 2022, **292**, 121038.

24 L.F. Hong, R.T. Guo, Y. Yuan, X.Y. Ji, Z.D. Lin, X.F. Yin and W.G. Pan, 2D Ti_3C_2 decorated Z-scheme $BiOIO_3$/g-C_3N_4 heterojunction for the enhanced photocatalytic CO2 reduction activity under visible light, *Colloids Surf., A*, 2022, **639**, 128358.

25 R.C. Wang, Y.C. Lin, H.C. Chen and W.Y. Lin, Energy harvesting from g-C_3N_4 piezoelectric nanogenerators, *Nano Energy*, 2021, **83**, 105743.

26 C. Yan, Z. Zhao, W. Jin, Q. Yu, J. Yu, J. Ran and X. Wang, Carbon quantum dots-doped g-C_3N_4 nanocomposites with enhanced piezoelectric catalytic performance, *Compos. Commun.*, 2023, **37**, 101466.

27 Z. Talebzadeh, M. Masjedi-Arani, O. Amiri and M. Salavati-Niasari, $La_2Sn_2O_7$/g-C_3N_4 nanocomposites: Rapid and green sonochemical fabrication and photo-degradation performance for removal of dye contaminations, *Ultrason. Sonochem.*, 2021, **77**, 105678.

28 Y. Guan, J. Pan and J. Fu, Constructing 0D/1D/2D Z-scheme heterojunctions of Ag nanodots/SiC nanofibers/g-C_3N_4 nanosheets for efficient photocatalytic water splitting, *Ceram. Int.*, 2023, **49**(2), 2262–2271.

29 S. Shenoy, C. Chuaicham and T. Okumura, Simple tactic polycondensation synthesis of Z-scheme quasi-polymeric g-C_3N_4/$CaFe_2O_4$ composite for enhanced photocatalytic water depollution via pn heterojunction, *Chem. Eng. J.*, 2023, **453**, 139758.

30 A. Ali, M. Amin and M. Tahir, g-C_3N_4/Fe_3O_4 composites synthesized via solid-state reaction and photocatalytic activity evaluation of methyl blue degradation under visible light irradiation, *Front. Mater.*, 2023, **10**, 1180646.

31 H. Li, D. Li and M. Long, Solvothermal synthesis of MIL-53Fe@ g-C_3N_4 for peroxymonosulfate activation towards enhanced photocatalytic performance, *Colloids Surf., A*, 2023, **658**, 130646.

32 X. Wang, X. Wang and W. Tian, High-energy ball-milling constructing P-doped g-C_3N_4/MoP heterojunction with MoN bond bridged interface and Schottky barrier for enhanced photocatalytic H_2 evolution, *Appl. Catal., B*, 2022, **303**, 120933.

33 Q. Zhao, S. Liu and S. Chen, Facile ball-milling synthesis of WO_3/g-C_3N_4 heterojunction for photocatalytic degradation of Rhodamine B, *Chem. Phys. Lett.*, 2022, **805**, 139908.

34 Q. Ding, X. Zou and J. Ke, S-scheme 3D/2D $NiCo_2O_4$@ g-C_3N_4 hybridized system for boosting hydrogen production from water splitting, *Renewable Energy*, 2023, **203**, 677–685.

35 J. Yang, C. Yu and S. Liang, Bridging of ultrathin $NiCo_2O_4$ nanosheets and graphene with polyaniline: a theoretical and experimental study, *Chem. Mater.*, 2016, **28**(16), 5855–5863.

36 C. Yan, Z. Zhao and W. Jin, Carbon quantum dots-doped g-C_3N_4 nanocomposites with enhanced piezoelectric catalytic performance, *Compos. Commun.*, 2023, **37**, 101466.

37 J. Jiang, X. Wang and C. Zhang, Porous 0D/3D $NiCo_2O_4$/g-C_3N_4 accelerate emerging pollutant degradation in PMS/vis system: Degradation mechanism, pathway and toxicity assessment, *Chem. Eng. J.*, 2020, **397**, 125356.

38 F. Yan, J. Kang and S. Zhang, Enhanced electromagnetic wave absorption induced by void spaces in hollow nanoparticles, *Nanoscale*, 2018, **10**(39), 18742–18748.

39 J. Jiang, W. Shi, F. Guo and S. Yuan, Preparation of magnetically separable and recyclable carbon dots/$NiCo_2O_4$ composites with enhanced photocatalytic activity for the degradation of tetracycline under visible light, *Inorg. Chem. Front.*, 2018, **5**(6), 1438–1444.

40 D. Liu, D. Chen and N. Li, Surface engineering of g-C_3N_4 by stacked BiOBr sheets rich in oxygen vacancies for boosting photocatalytic performance, *Angew. Chem., Int. Ed.*, 2020, **59**(11), 4519–4524.

41 M. Jourshabani, M.R. Asrami and B.K. Lee, Advanced Functional Carbon Nitride by Implanting Semi–Isolated VO_2 Active Sites for Photocatalytic H_2 Production and Organic Pollutant Degradation, *Small*, 2023, **19**, 2300147.

42 J. Ran, H. Chen and X. Bai, Immobilizing CuO/$BiVO_4$ nanocomposite on PDA-templated cotton fabric for visible light photocatalysis, antimicrobial activity and UV protection, *Appl. Surf. Sci.*, 2019, **493**, 1167–1176.

43 J. Zou, X. Tang, L. He, W. Jin, Q. Yu, J. Yu and D. Cheng, Metal-organic framework derived N–doped zinc oxide carbon nanocomposites for catalytic removal of dye and formaldehyde, *Polym. Compos.*, 2024, **45**(2), 1024–1035.

44 W. Chang, W. Xue, E. Liu, J. Fan and B. Zhao, Highly efficient H_2 production over $NiCo_2O_4$ decorated g-C_3N_4 by photocatalytic water reduction, *Chem. Eng. J.*, 2019, **362**, 392–401.

45 J. Fu, Q. Xu, J. Low, C. Jiang and J. Yu, Ultrathin 2D/2D WO_3/g-C_3N_4 step-scheme H_2-production photocatalyst, *Appl. Catal., B*, 2019, **243**, 556–565.

46 S. Gong, W. Zhang and Z. Liang, Construction of a $BaTiO_3$/tubular g-C_3N_4 dual piezoelectric photocatalyst with enhanced carrier separation for efficient degradation of tetracycline, *Chem. Eng. J.*, 2023, **461**, 141947.

47 D. Xu, T. Yang and Y. Dong, Activation of peroxymonosulfate by CoP@Co_2P heterostructures via radical and non-radical pathways for antibiotics degradation, *Ceram. Int.*, 2023, **49**(11), 16999–17007.